# Tides in the Casamance estuary: A modeling study

Birane Ndom, Siny Ndoye, Bamol Ali Sow, Vincent Echevin

Continental Shelf Research 285 (2025) 105389

Contents lists available at ScienceDirect

Continental Shelf Research

journal homepage: www.elsevier.com/locate/csr

# Tides in the Casamance estuary: A modeling study

Birane Ndom [a,b], Siny Ndoye [c], Bamol Ali Sow [b], Vincent Echevin [a,*]

[a] Laboratoire d'Océanographie et de Climatologie: Expérimentation et Approches numériques (LOCEAN), Sorbonne Université, CNRS/IRD/MNHN/SU, Paris, France
[b] Laboratoire d'Océanographie, des Sciences de l'Environnement et du Climat (LOSEC), Université Assane Seck, Ziguinchor, Senegal
[c] UFR Sciences et Technologies Avancées (STA), Université Amadou Mahtar Mbow (UAM), Dakar, Senegal

A B S T R A C T

The Casamance estuary, located in southern Senegal, is a region of remarkable ecological, tourist and economic significance. It undergoes strong seasonal variations of salinity due to its reverse estuary nature during the dry season. This study aims to characterize tidal dynamics in the western part of the Casamance estuary, spanning from the river mouth to the town of Ziguinchor, during the dry season. Utilizing a three-dimensional, non-linear model with a high spatial resolution, we focused on simulating the tidal elevations and currents and evaluating them with sea level and current measurements both within the estuary and at its mouth. Whereas modelled tidal elevations agreed with observations, revealing eastward tidal propagation within the estuary, tidal currents near the river mouth and into the estuary were underestimated. The Eulerian residual circulation was mainly seaward whereas the Lagrangian residual circulation was significantly weaker due to compensation by the Stokes drift. This modeling study marks a crucial first step towards conducting comprehensive environmental impact assessments in the Casamance estuary, paving the way for a deeper understanding and preservation of this region.

## 1. Introduction

Estuarine regions have significant socio-economic potential, but also face a wide range of environmental issues. Estuaries are links between land and ocean, where freshwater from rivers mixes with salty ocean water. The hydrodynamics of these systems has been the subject of significant research for decades (*e.g.,* Geyer and MacCready, 2014 for a review), drawing on theoretical approaches (*e.g.,* Burchard et al., 2011), numerical modeling (*e.g.,* Marchesiello et al., 2019; Minh et al., 2014a; Piton et al., 2020a,b) and observations (*e.g.,* Nuñes et al., 1990).

Bordered to the north by Gambia, to the south by Guinea Bissau and to the west by the Atlantic Ocean, the Casamance region is located in the rainiest area of Senegal and drains a watershed located at the southernmost tip of Senegalese territory (Fig. 1). The Casamance estuary plays an important role in the country's economy: it holds an ecosystem lined with mangroves and highly productive in terms of fishery resources, with numerous artisanal shrimp fisheries (Le Reste, 1982; Ziegler et al., 2009), much in demand for river navigation (*e.g.,* daily connections between Dakar and Ziguinchor) and tourism (Diombéra, 2010; Sène and Diémé, 2018). In addition, the regions bordering the river are exploited in the form of rice fields (FAO, 2011). The main branch of the Casamance River is 220 km long (Diouf et al., 1986). The channel is around 3 km wide and 20 m deep towards the mouth. At Ziguinchor, 75 km from the coast, the channel is around 700 m wide and 10 m deep.

This semi-enclosed basin functions as a negative or inverse estuary during the dry season (December–May) (Savenije and Pagès, 1992; Descroix et al., 2020). Inverse or low-inflow estuaries are characterized by a positive downstream-upstream salinity gradient, with evaporative water loss exceeding freshwater river runoff and precipitation (*e.g.,* Nuñes et al., 1990; Largier, 2023). The salinity of estuarine water thus significantly exceeds that of seawater. Estuaries are areas of intense mixing between freshwater from rivers and salty oceanic water, particularly under the influence of the tide (Geyer and MacCready, 2014). The tide is also one of the main factors influencing estuarine circulation. In particular, spring tides are responsible for strong vertical mixing and a high concentration of suspended solids (*e.g.,* Schoellhamer (2000) in the bay of San Francisco). During the rainy season (June–September), the Casamance basin is fed by numerous smaller tributaries such as the Soungrougrou, Niamone and Elinkin (Descroix et al., 2020).

The tide in the Casamance estuary has been little studied in the past. Apart from occasional measurements of water height (Brunet-Moret, 1970), to our knowledge the only tidal modeling study was carried out by Lahoud (1989), in the eastern zone of the Casamance estuary (between Ziguinchor and Kolda, located ~75 km and ~260 km from the mouth respectively). The amplitude and phase of the most important semi-diurnal (M2, S2, N2, K2) and diurnal (K1, O1) components were reproduced with a model forced by the tidal signal at Ziguinchor. Millet et al. (1986) observed the rapid reversal of flood and ebb tidal currents

* Corresponding author.
*E-mail address:* vincent.echevin@locean.ipsl.fr (V. Echevin).

https://doi.org/10.1016/j.csr.2024.105389
Received 6 June 2024; Received in revised form 29 November 2024; Accepted 8 December 2024
Available online 13 December 2024

in several locations along the river. Nevertheless, water levels and tidal currents in the western part (*i.e.,* west of Ziguinchor) of the Casamance estuary have not been studied using a hydrodynamical model.

The aim of this study is to simulate the characteristics of tidal dynamics in the western part of the Casamance estuary using a high-resolution regional ocean circulation model evaluated with in-situ and satellite data. We focus on the dry season, thus there is no outward freshwater flow in the estuary.

The paper is organized as follows: section 2 presents the study area, the *in-situ* and satellite observations, the hydrodynamic model and the configurations that were used, the methodology for model validation and tidal analysis. Section 3 presents the model-observation comparisons and the model results. The latter are discussed in section 4. Section 5 presents the conclusions and perspectives of this study.

## 2. Material and methods

### 2.1. Circulation model

The Coastal and Regional Ocean COmmunity model (CROCO; Hilt et al., 2020) was used to simulate the tide in the Casamance estuary. CROCO solves the primitive equations coupled with conservation equations for temperature, salinity and momentum. A nonlinear density equation of state, the Boussinesq approximation and the hydrostatic assumption in the conservation of momentum on the vertical were used (Shchepetkin and McWilliams, 2005). The Adaptative Grid Refinement In Fortran (AGRIF; Debreu et al., 2012) nesting tool was used to resolve very fine spatial scales in the estuary. A virtual salt flux formulation (Roullet and Madec, 2000) was used to simulate the effect of water fluxes (by evaporation and precipitation) on salinity. The virtual salt flux was parameterized as a surface boundary condition for salinity vertical diffusion: $K_z\partial_z S|_{z=0} = (E\text{-}P)SSS$ with $K_z$ the vertical mixing coefficient, E the evaporation, P the precipitation and SSS the model surface salinity. Details on (E-P) are given in section 2.4.

For current bottom friction, a logarithmic parameterization of the friction coefficient ($C_D$) allowing spatial variation was used ("law of the wall", von Karman, 1931, Equation (1)):

$$C_D = \left[\frac{\kappa}{\ln(Z_b/Z_0)}\right]^2 \quad (1)$$

with $\kappa = 0.41$ the Von Karman constant, $Z_0$ the roughness length, $Z_b$ the reference height in the bottom layer at which bottom velocity is computed, equal to half the thickness of the bottom layer. The non-local "K profile parameterization" (KPP) scheme (Large et al., 1994) was used for vertical mixing.

Open boundary conditions are needed for the boundaries facing the open ocean. Baroclinic variables (temperature, salinity and velocity)

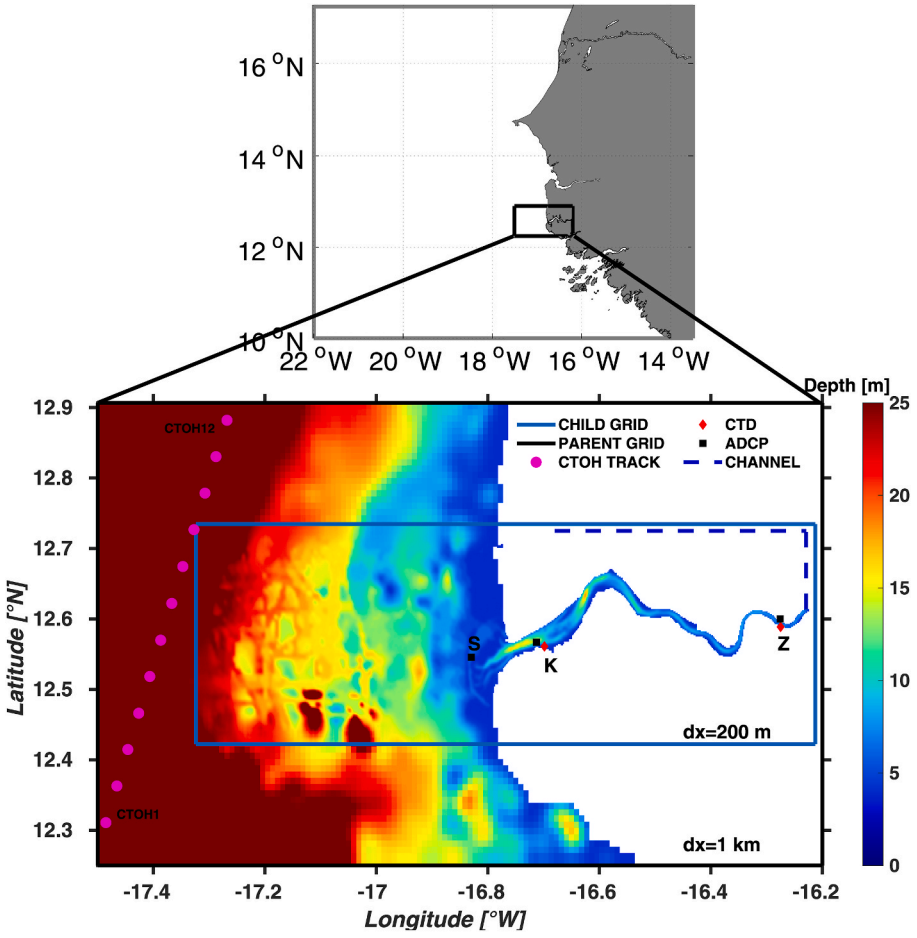


**Fig. 1.** Location of the Casamance estuary, model domains, satellite and in-situ observations. The low-resolution parent grid (CASAM1; 1 km horizontal resolution) is indicated by a black rectangle and the high-resolution child zoom (CASAM200; 200m horizontal resolution) is indicated by a blue rectangle. X-TRACK satellite altimetric sea level data supplied by the Centre d'Etudes Topographiques de l'Océan et de l'Hydrosphère (CTOH) are indicated by 14 purple dots. CTOH1 and CTOH12 mark satellite data locations close to CASAM1 open boundaries. Satellite tidal elevations at these locations were compared to those of the TPXO7 global model forcing CASAM1 (see Fig. S3). CTD positions are indicated by red diamonds at Karabane Island pier (K) and Ziguinchor pier (Z). ADCP positions are indicated by black squares. S indicates the position of the ADCP mooring on the shelf. The dashed blue line indicates the orientation and length of the channel located at the upstream part of the estuary. (For interpretation of the references to color in this figure legend, the reader is referred to the Web version of this article.)

were imposed via an adaptative radiation condition (Marchesiello et al., 2001) allowing perturbations to leave the model domain without affecting the interior solution. For barotropic forcing, the incoming characteristic of the shallow-water equations was applied, allowing the propagation of tidal waves into the domain (Marchesiello et al., 2001; Blayo and Debreu, 2005). More specifically, only the tidal elevation (i.e., not the tidal barotropic currents) was used to force the tidal signal into the model domain (for more details, see https://www.croco-ocean.org).

### 2.2. Model configuration

Two model grids were used: a "parent" grid (CASAM1) and a "child" grid (CASAM200), nested within the parent grid using AGRIF. CASAM1 covers the southern part of Gambia, the southern part of Senegal and northern Guinea-Bissau in latitude (12°15′-12°54′N), and the Casamance estuary between the river mouth and east of Ziguinchor in longitude (17°30′-16°11′60″W; Fig. 1), with a horizontal resolution of 1 km. CASAM200 covers the Casamance estuary as far as Ziguinchor (12°25′-12°44′N; 17°19′-16°12′W) with a horizontal resolution of 200 m. On the vertical, the water column was discretized into 10 sigma levels with no surface or bottom refinement ($\theta s = \theta b = 0$; see Penven et al., 2008). A time-splitting algorithm was used: the barotropic and baroclinic time steps for CASAM1 (CASAM200) grid were equal to 1.5 s and 90 s (0.3 s and 18 s), respectively.

The bathymetry used was taken from the GEBCO_2021 database (GEBCO, 2021). This database provided depth data (in meters) on a 15 arc-second grid. GEBCO data was used for bathymetry in the oceanic zone (west of 16.75°W). In the estuarine zone, GEBCO and a bathymetric dataset from Rijksdienst Voor Ondernemend (hereafter RVO), acquired by ADCP during the Ziguinchor port site survey campaign (Brak et al., 2013), were merged. RVO data was obtained by surveying along lines spaced at least 200 m apart (near the mouth) to 400 m apart (in the estuary; Fig. S1). RVO data was first interpolated onto the GEBCO grid every 15'' (Fig. S2). The merged bathymetry was then interpolated on the CROCO grid and smoothed with a Hanning filter to obtain an r ratio ($r = \delta h/h$) of less than 0.4 to avoid pressure gradient errors. The minimum depth of the model topography was set at 4 m, and intertidal salt marshes were not represented (Fig. 1). In addition, in order to simulate the effects of tidal wave propagation and dissipation associated with the unrepresented part of the river east of Ziguinchor, an idealized channel 56 km long, 3 km wide and 4 m deep was connected to the river. The channel length is expected to have an impact on the tidal currents and residual circulation (Li and O'Donnel, 2005). Sensitivity tests were carried out to estimate the optimal length of the channel (see section 2.7). As no river discharge was taken into account in the present study (focusing on the dry season), the upstream boundary condition at the end of the channel is a closed boundary.

### 2.3. Tidal forcing

CROCO has been used to simulate the tide in several coastal regions of the global ocean (*e.g.,* Minh et al., 2014; Marchesiello et al., 2019; Dinapoli et al., 2020; Sow et al., 2021), including the South Senegalese upwelling region (Ndoye, 2016; Ndoye et al., 2017). Tides in the Casamance were studied in the 1970s for the first time (Brunet-Moret, 1970; Lahoud, 1989). These authors estimated the amplitudes and phases of the main diurnal (K1, O1, P1, Q1) and semi-diurnal (M2, S2, N2 and K2) harmonics near the river mouth and near Ziguinchor, along with the quarter-diurnal M4 constituent resulting from nonlinear M2-M2 nonlinear interactions. The forcing of diurnal and semi-diurnal tidal harmonics imposed at the model's open boundaries should therefore provide a relatively complete representation of the tide in the estuary.

The amplitude and phase of each tidal component for elevation from the 1/4° TPXO7 global tidal model (Egbert and Erofeeva, 2002) were interpolated along the open boundaries of the parent grid. To evaluate TPXO7 sea level variations in the region of interest, model solutions were compared with satellite altimetric data from the X-TRACK product (Birol et al., 2017) at positions CTOH1 and CTOH12 close to the model boundaries (see Fig. 1). The amplitude and phase errors of the main tidal waves M2 (1% and 3% on amplitude; 20.1° and 21.8° on phase respectively for CTHO1 and CTOH12) and S2 (5% and 3% on amplitude and 3.5° and 2.3° on phase respectively for CTHO1 and CTOH12; Fig. S3) were relatively small, despite a slight phase shift during the neap tide (Fig. S2). Overall, we considered that the TPXO7 product represented sufficiently well the tidal signal off Casamance and was thus appropriate to force the model at open boundaries.

### 2.4. Seasonal oceanic and atmospheric forcings

Tides were added to a monthly climatological oceanic forcing: temperature, salinity and geostrophic currents (computed using a reference level at 1000 m depth) from the World Ocean Atlas climatology (Levitus et al., 2010), interpolated to the model boundaries. January was used for initial conditions. Nearshore ocean temperature and salinity conditions were extrapolated into the estuary thus initial conditions were nearly homogeneous in the estuary.

Momentum fluxes were imposed at the model air-sea interface. The SCOW (Scatterometer Climatology of Ocean Winds, 1999–2009; Riesen and Chelton, 2008) satellite wind stress climatology at 25 km resolution was interpolated onto the model grids. Monthly winds were used so that the synoptic (1–10 days) to diurnal variability was neglected. No bulk parameterization was used so that the imposed wind stress did not take into account the effects of the model SST and surface velocity.

Heat (solar and net) and net freshwater (E-P) fluxes from the COADS climatology (Da Silva et al., 1994) were prescribed. Note that evaporation (E) was not computed from latent heat flux as no bulk formulation was used. Restoring to climatological SST and SSS (with a time scale of ~10 days) was also included, following Barnier et al. (1995) parameterization. Nevertheless, prescribing freshwater fluxes and restoring to climatological surface fields had a weak impact on the circulation in the estuary (see section 3.5).

As SCOW and COADS climatological data was not available in the estuary, nearshore oceanic data was extrapolated landward over the river grid points. Pre-processing and interpolation on the model grids were carried out using CROCO_TOOLS software (Penven et al., 2008; https://www.croco-ocean.org/).

Several simulations were then performed: the "reference" simulation included tidal and climatological atmospheric and oceanic forcing, the "noatm" simulation included tidal forcing only, and the "notide" simulation included climatological atmospheric and oceanic forcing only. The simulations characteristics are summarized in Table 1.

### 2.5. Lagrangian modeling

The long-term estuarine transport of organic or dissolved matter is generally dominated by the tidal residual signal, averaged over a large number of tidal cycles. Its nature is therefore strongly Lagrangian. The

**Table 1**
Characteristics of the simulations (name, duration, and forcings).

| simulation name | Duration | tidal forcing (TPXO7) | wind stress (SCOW) | heat flux (COADS) | freshwater flux (COADS) |
|---|---|---|---|---|---|
| reference | 1 January-June 30, 2012 | X | X | X | X |
| noatm | 1 January-June 30, 2012 | X | – | – | – |
| notide | 1 January-June 30, 2012 | – | X | X | X |

Lagrangian velocity is equal to the sum of the Eulerian velocity and the Stokes drift associated with gravity and surface waves (Longuet-Higgins, 1969). While wind-driven surface waves were not represented in our simulation, tidal waves and other higher-frequency gravity waves may propagate into the model domain. A Lagrangian particle-tracking method using the ROFF Lagrangian model (ROMS Offline Floats; Carr et al., 2008) was used to compute Lagrangian velocities. Particles were released at the center of each CASAM200 mesh (1260 in total) in the surface layer (at 0.1 m depth) and advected by hourly Eulerian currents from the reference simulation. The positions (longitude, latitude and depth) of the particles were recorded every hour. Several Lagrangian experiments were carried out.

- a single one-month particle tracking simulation over the period February–March was carried out using the reference simulation hourly currents. The aim of this experiment was to highlight particle trajectories at different locations in the estuary.
- Particle tracking simulations for a time period of 14.7 days (half a lunar month) were launched every 3 h from February 1, 2012 to May 10, 2012 (*i.e.,* a total of 800 experiments). These experiments were carried out using currents from the "noatm" simulation (*i.e.,* with tidal forcing only; see Table 1). They accounted for the influence of neap-spring variations on the residual currents. Lagrangian velocities were calculated using the trajectories of the released particles: the distance between initial and final positions was divided by the elapsed time. The final positions of the particles at the end of the tracking (*i.e.,* after 14.7 days) were used only for the particles that were not stranded (the trajectories of the stranded particles were not considered). The origin of each Lagrangian velocity vector was chosen to be the model grid point closest to the median position of the particle along its trajectory. Lagrangian velocity fields were calculated for each release and then averaged over either all the releases (800) or over the releases corresponding to the same phase of the dominant M2 tide (200 releases for each case: 0h, 3h, 6h, 9h). Note that the Lagrangian velocities we built are pure kinematic computation without any reference to a mass conservation.

### 2.6. In-situ data

#### 2.6.1. Sea level

Sea level data was derived from two CTD pressure measurements (Descroix et al., 2020). The CTDs were placed in the harbor of the island of Karabane (2 km from the river mouth) and at Ziguinchor (70 km from the river mouth; Fig. 1). Pressure data was provided every 10 min from January to December 2019 at Karabane and from February to October 2016 at Ziguinchor. Effects of the atmospheric pressure variability on sea level were corrected using sea level pressure from the ERA5 reanalysis (Hersbach et al., 2020).

#### 2.6.2. Currents

Several moorings equipped with ADCP current meters were installed in Casamance (Fig. 1), over different time periods. A first mooring set up by RVO (see label S in Fig. 1) was equipped with a Nortek AWAC ADCP (Brak et al., 2013) and moored over the shelf at the river mouth at a depth of around 6 m from November 11 to December 2, 2012. Two other moorings equipped with an Aquadopp 1000 kHz ADCP were installed off the island of Karabane (November 23–24, 2021, 14 m depth, see label K in Fig. 1) and at Ziguinchor (November 21–22, 2021, 9 m depth; Machu E. and Capet X., personal communication, see label Z in Fig. 1). Old current measurements at Ziguinchor (March 25, 1985; Millet et al., 1986) were also used. All these measurements were used to assess the intensity, variability and vertical structure of the simulated currents.

To enable a more accurate comparison with the data, simulations were produced for each of the observation periods (Table 2). Each simulation consisted of hourly outputs of sea level and currents at each level. The root-mean-square error (RMSE) provided a quantitative estimate of the difference between measured and modelled water levels over a given period.

The t_tide software (Pawlowicz et al., 2002) was used to extract the amplitude (in meters), phase (in degrees, the time reference being January 1, 0000) and associated error bars of each tidal wave, for the observations and at each model grid point.

### 2.7. Sensitivity studies

#### 2.7.1. Idealized channel length

Several idealized channel length values were tested in the CASAM1 configuration (without nesting). Sea levels at Ziguinchor and Karabane were simulated and compared with observations. A reduction in RMSE was observed as channel length increased: RMSE at Ziguinchor was 0.17 cm (resp. 0.09 cm) for a 45 km (resp. 56 km) channel, a reduction of 48%; RMSE at Karabane was 0.15 cm (resp. 0.10 cm) for a 45 km (resp. 56 km) channel, a reduction of 32%. Note that these tests were carried out with a roughness length of $Z_o = 100$ mm. A channel length of 56 km was then used in the CASAM200 simulation.

#### 2.7.2. Bottom friction

Current-bottom friction is a major tidal energy dissipation process in shallow estuarine zones. Different parameterizations have been tested to better represent tidal dynamics in different study areas (*e.g.,* Piton et al., 2020a,b; Qian et al., 2021; Sow et al., 2021). Following this approach in our study area, a logarithmic parameterization of the friction coefficient ($C_D$) allowing spatial variation was used (see Equation (1) in section 2.1). Different values of the roughness length $Z_o$ were tested in order to minimize the deviation from water level observations.

**Table 2**
Simulations produced for comparison to the observations available over different observation periods. All simulations are based on a child grid of 200 m horizontal resolution and 10 equally spaced sigma levels in the vertical. Boundary conditions and atmospheric forcing correspond to those of the reference simulation (Table 1).

| Simulation name | casam200-Mar1985 | casam200-Nov2012 | casam200-Feb2016 | casam200-Feb2019 | casam200-2012 |
|---|---|---|---|---|---|
| Time period | Feb–Mar 1985 | Oct–Nov 2012 | Jan–Jun 2016 | Jan–Jun 2019 | Jan–Dec 2012 |
| Roughness length ($Z_o$, in mm) | 80 | 80 | 80 | 80 | 80 |
| Objective | Comparison to currents at Ziguinchor | Comparison to "Shelf point" currents | Comparison to sea level at Ziguinchor | Comparison to sea level at Karabane | Eulerian and Lagrangian residual currents |
| Simulation name | casam200a-Nov 2021 | casam200b-Nov 2021 | | | |
| Time period | November 2021 | November 2021 | | | |
| Roughness length ($Z_o$, in mm) | 80 | 10 | | | |
| Objective | Comparison to currents at Z. and K. | Comparison to currents at Z. and K. | | | |

## 3. Results

### 3.1. Calibration of bottom friction

This section focuses on analyzing the sensitivity of water levels (at Karabane and Ziguinchor) to bottom friction parameterization. The sensitivity simulations consisted in varying the roughness length ($Z_o$) used in the friction parameterization. Table 3 shows RMSE as a function of $Z_o$ at Karabane and Ziguinchor, and the mean RMSE. RMSE decreased with increasing roughness length at both measurement points. A minimum was reached for $Z_o = 50$ mm in Karabane and $Z_o = 70$–100 mm in Ziguinchor. The lowest mean RMSE was obtained for $Z_o = 80$ mm, the value used in the reference simulation analyzed in the following sections, unless mentioned otherwise.

### 3.2. Model sea level evaluation

Sea level data was used to evaluate the model sea levels obtained from the various simulations. Fig. 2 shows the time series of modelled and observed sea level near the river mouth ("Shelf" point) in November 2012 (a), at Karabane in February 2019 (b) and at Ziguinchor in February 2016 (c). The low-frequency signal was filtered by subtracting a 3-day moving average. At Karabane (Fig. 2b), the tidal signal was semi-diurnal, its range varying from a neap minimum (~0.6 m) around February 14 to a spring maximum (~1.2 m) around February 6 and February 21. In Ziguinchor (Fig. 2c), there was little variation in tidal range (~0.6 m) between spring and neap periods. Offshore of the estuary (Fig. 2a), the tidal range was greater (~2 m during spring tide and ~1 m during neap tide).

### 3.3. Vertical structure of the zonal current

We examined the vertical structure of the current and its temporal variations over a semi-diurnal tidal cycle (~12 h) at Karabane and Ziguinchor (Fig. 3). As the zonal current was nearly oriented along-channel and thus more intense than the meridional current, only this component was considered.

At Karabane (Fig. 3a), the observed current at 4m (resp. 14m) depth reached ~50 cm $s^{-1}$ (resp. ~25 cm $s^{-1}$) during flood (eastward current at 0:00 and 12:00) and ~90 cm $s^{-1}$ (resp. ~50 cm $s^{-1}$) during ebb (westward current at 6:00). This asymmetry could be linked to the relatively intense river runoff during this time period (November 2021), just after the rainy season. Nonlinear mechanisms such as advection, bottom friction (Parker, 1991) or coupling between wind waves and barotropic tides (Rickerich et al., 2022) can also produce tidal asymetries (overtide) resulting from higher frequency harmonics. However asymmetry on sea level was weak at Karabane (see section 3.4 for more details). Consequently, we estimated roughly the amplitude of the tidal current assuming a constant river discharge ($U_b$) over the short observation period (~1 day), and a semi-diurnal tidal flow. We obtained $U_b \sim (U(t = 0{:}00) + U(t = 6{:}00))/2$–20 cm $s^{-1}$ at 4 m depth. Similarly, the estimated amplitude of the tidal current was ~60 cm $s^{-1}$. The model reproduced well the temporal variability of the current, with a reversal in the direction of the current from ebb to flood between 12:00 and 15:00 (Fig. 3b). However, the amplitude of the simulated current (~20 cm $s^{-1}$) was underestimated. This low value could reduce nonlinearities and overtides (see section 3.4).

Zonal currents measured at Ziguinchor (in November 2021, after the rainy season) during flood (0:00–3:00) and ebb (6:00–9:00) were less asymmetrical than at Karabane, and of the order of $\sim \pm 50$ cm $s^{-1}$ at 4m depth (Fig. 3d). Older measurements (Millet et al., 1986; Fig. 3g) collected during the dry season (March 1985) at Ziguinchor in the middle of the channel (10 m depth) were slightly stronger than those measured in November 2021, possibly due to the larger depth and reduced bottom friction. The circulation was also slightly less asymmetrical in March (Fig. 3g) than in November (Fig. 3d), possibly due to the weaker seaward (westward) flow during the dry season. For both time periods, the model represented well the variability of the current, but underestimated its amplitude (Fig. 3e and h). Lastly, the model's underestimation of tidal currents was confirmed by comparing the simulated and observed currents at the "Shelf" point located at a depth of 4.4 m near the river mouth (see label S in Fig. 1). The model reproduced the zonal velocities fairly well, but clearly underestimated the amplitude of the current oscillations (Fig. 4). A phase shift between model and data was also visible during neap tides (*e.g.*, November **19–21, 2012).**

To assess the sensitivity of tidal current amplitude to bottom friction, a model simulation with lower bottom friction (*i.e.,* roughness length ($Z_o$) of 10 mm) was carried out. An increase in maximum current intensity of ~20% (*e.g.,* at t = 0:00) was found at Karabane (Fig. 3c) and of ~40% at Ziguinchor (Fig. 3f). Nevertheless the modelled currents remained weaker than the observed and tidal elevations were less realistic than in the reference simulation (see Table 3).

In conclusion, the model represented the vertical structure and variability of tidal currents fairly well, but underestimated their intensity by around 50%.

### 3.4. Characterization of the main tidal components

The spatial distribution of amplitudes and phases of the two main tidal components (M2 and S2) in Casamance is shown in Fig. 5. The other semi-diurnal (N2) and diurnal (O1,K1,Q1) components had much lower amplitudes (Fig. S4). The increase in phase towards the east indicates that M2 and S2 propagate eastward. Based on the tidal phase patterns, its takes less than 3h (~2.6h for M2 and ~2.8h for S2) for the tidal wave to propagate along the estuary from the river mouth to Ziguinchor. The amplitude isolines were perpendicular to the shores of the estuary. The amplitude of M2 (resp. S2) decreased upstream from 56 cm (resp. 18 cm) at the "Shelf" point near the river mouth to 18 cm (resp. 6 cm) near Ziguinchor. M2 (resp. S2) amplitude also decreased upstream along the idealized channel, reaching 8.6 cm (resp. 2.4 cm) ~43 km from Ziguinchor (not shown). These amplitudes were relatively close to those obtained from the Kaour tide gauge located 43 km upstream of Ziguinchor (M2: 10.7 cm; S2: 1.8 cm; Lahoud, 1989), indicating that tidal dissipation in the channel was correctly represented.

Because of semi-diurnal tide dominance (M2), the most significant overtide is expected to be the quarter-diurnal tide M4, which usually arises from nonlinearities in the continuity equation, advection, and the depth effect on bottom friction. These nonlinearities can generate asymmetries in the durations of the sea level rise (flood) and fall (ebb). Here, the duration of the ebb and flood were computed directly from the sea level time series. Ebb duration corresponds to the time between a sea level maximum and its following minimum. The time between a sea level minimum and its following maximum gives the flood duration (this analysis could not be carried out with the current measurements because

**Table 3**
Root-mean-square error (RMSE, **in m**) computed from modelled and observed sea level for sensitivity tests carried out by varying the values of bottom roughness $Z_o$ (in mm, uniform over the domain).

| Zo (in mm) | 1 | 10 | 20 | 30 | 40 | 50 | 60 | 70 | 80 | 90 | 100 |
|---|---|---|---|---|---|---|---|---|---|---|---|
| RMSE Karabane | 0,143 | 0,115 | 0,105 | 0,100 | 0,099 | 0,097 | 0,098 | 0,099 | 0,100 | 0,101 | 0,102 |
| RMSE Ziguinchor | 0,170 | 0,158 | 0,140 | 0,127 | 0,117 | 0,109 | 0,104 | 0,101 | 0,100 | 0,099 | 0,99 |
| Mean RMSE | 0,158 | 0,137 | 0,123 | 0,114 | 0,108 | 0,103 | 0,101 | 0,100 | 0,100 | 0,100 | 0,100 |

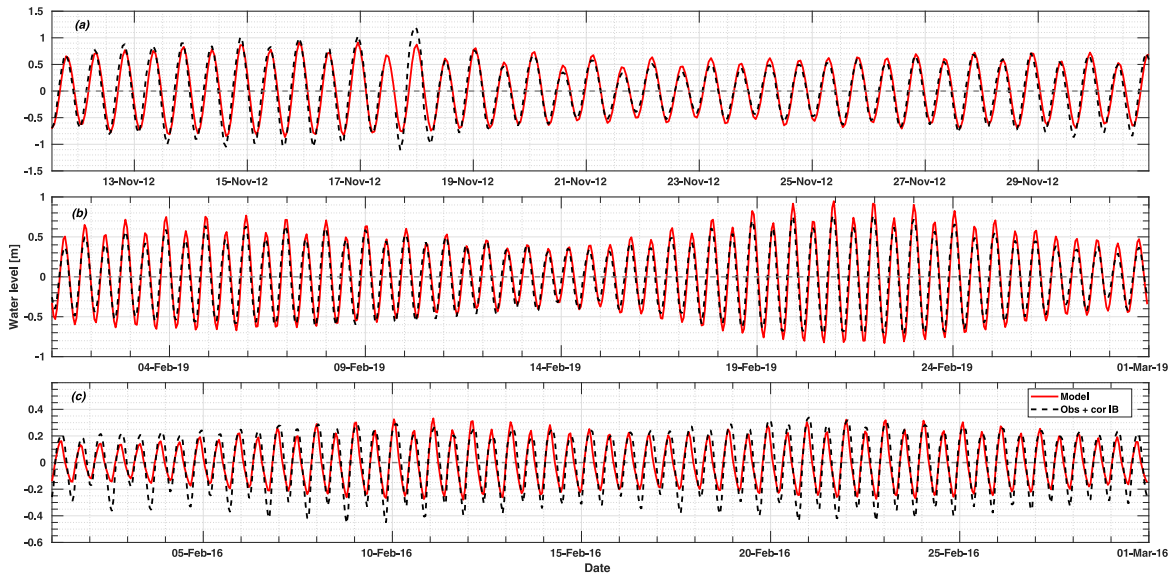


**Fig. 2.** Time series of observed (black line) and modelled sea level anomaly (red dashed line, reference simulation, see Table 1) at various locations: (a) at the river mouth (label S in Fig. 1) in November 2012, (b) at Karabane (label K in Fig. 1) in February 2019 and (c) at Ziguinchor (label Z in Fig. 1) in February 2016. Effects of atmospheric variability on observed sea level were corrected using ERA5 sea level pressure. (For interpretation of the references to color in this figure legend, the reader is referred to the Web version of this article.)

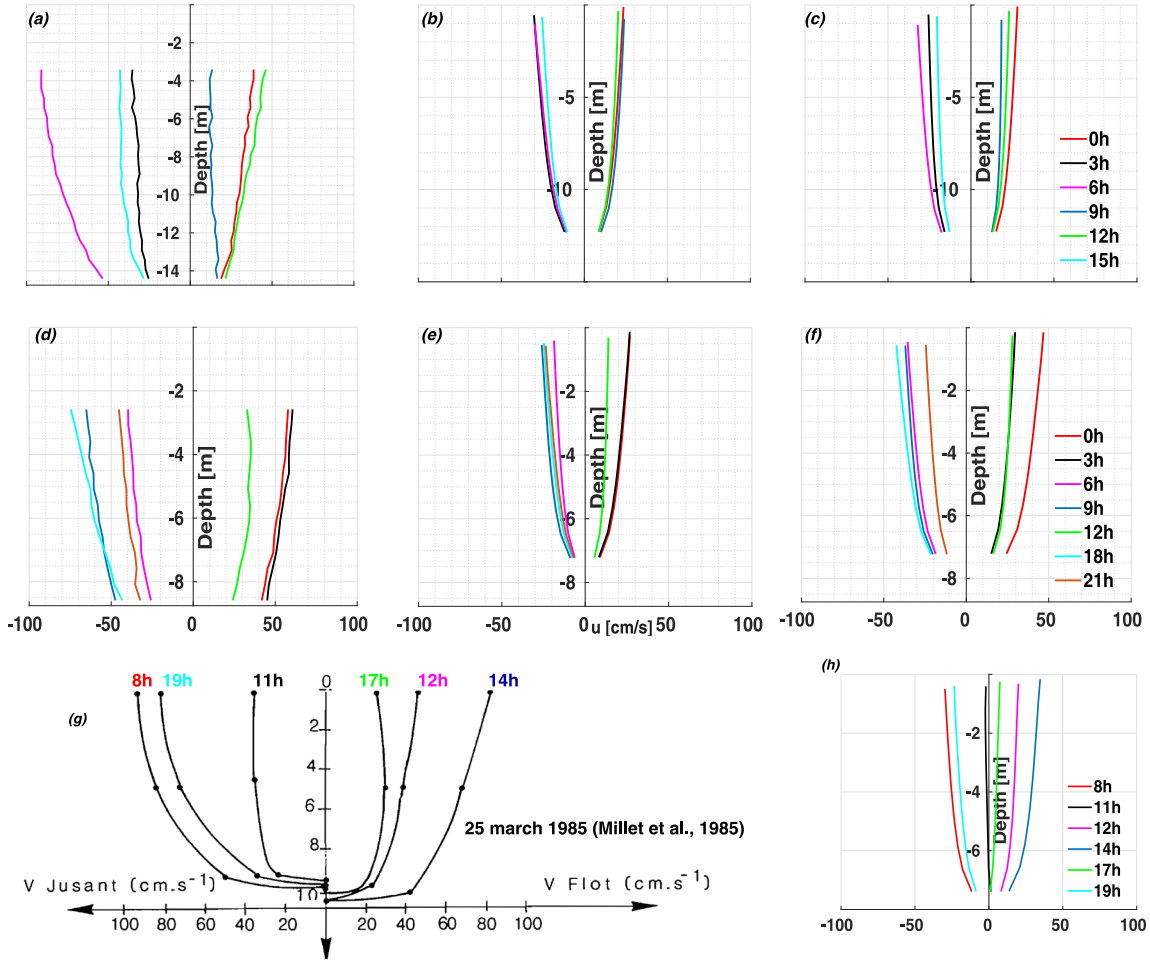


**Fig. 3.** Vertical structure and temporal variability of the zonal current over a tidal cycle: (a,b,c) on 2021-11-24 at Karabane and (d,e,f) between 2021 and 11-21:18:00 and 2021-11-22:18:00 (after the rainy season) and (g) 1983-03-25 (during the dry season) at Ziguinchor: (a,d,g) observations; (b,e,h) currents modelled with $Z_o = 80$ mm; (c,f) currents modelled with $Z_o = 10$ mm.

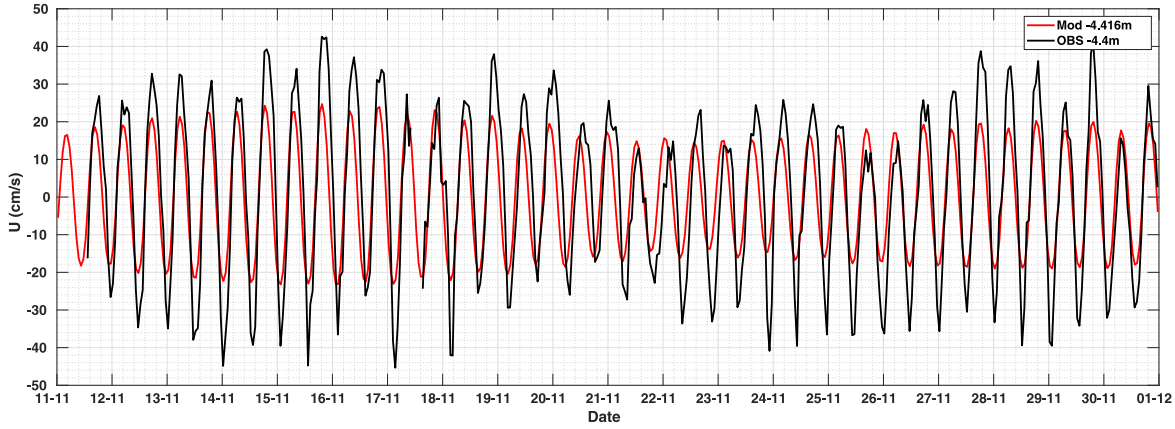


**Fig. 4.** Zonal current at 4.4 m depth at the "Shelf" point (label S in Fig. 1): model (red line; reference simulation) and observations (black line) between November 11, 2012 and November 27, 2012. (For interpretation of the references to color in this figure legend, the reader is referred to the Web version of this article.)

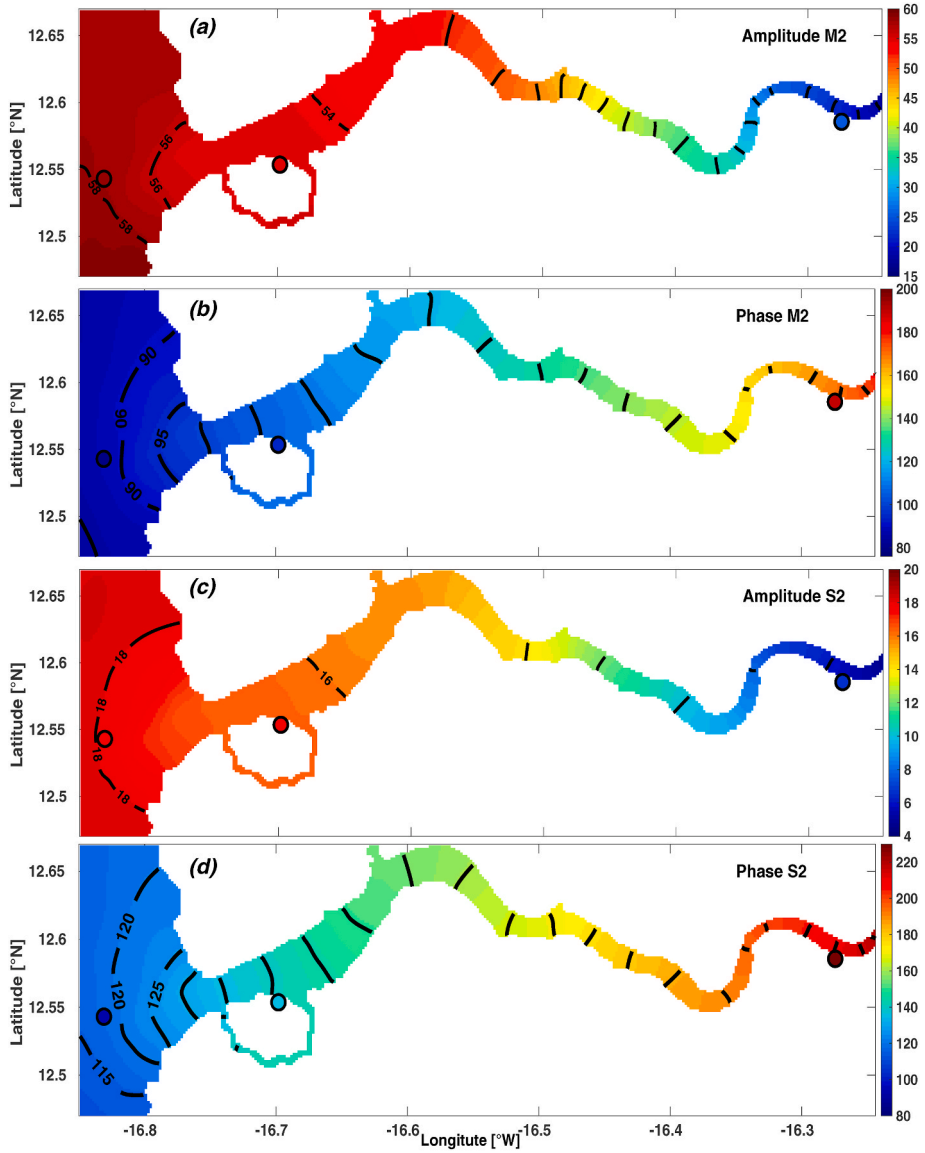


**Fig. 5.** Amplitude (in cm) and phase (in degrees) of the main tidal components: M2 (resp. a and b) and S2 (resp. c and d). Circles in each panel indicate amplitude and phase derived from observations over the shelf, at Karabane and Ziguinchor.

the time series were too short). A shorter flood duration (*i.e.,* flood dominance) near the river mouth (Karabane, ~0.5–1h; Fig. S5b) and in the estuary (Ziguinchor, ~1–2 h; Fig. S5d) were simulated by the model, while observations at these locations were inconclusive (Figs. S5a and c).

Following Friedrichs and Aubrey (1988), we also computed the ratio r of M4 amplitude to M2 amplitude, and the phase of the quarter-diurnal tide relative to M2, defined as $\Delta\varphi = 2\varphi(M4)-\varphi(M2)$. Relatively weak ratios were found near the river mouth ($r_{model}$~0.02 and $r_{obs}$~0.03 at Karabane; Table 4). Nonlinearities were stronger in the estuary ($r_{model}$~0.05 and $r_{obs}$~0.14 at Ziguinchor). Note that the observed amplitude of M4 at Ziguinchor was higher (3.7 cm; Table 4) than previously estimated (2.9 cm; Lahoud (1989)). The MS4 (resp. S4) quarter-diurnal tidal constituent was slightly weaker (resp. much weaker) than M4 (Fig. S4).

### 3.5. Tidal circulation

The model was able to reproduce surface and deep tidal circulation with a certain degree of realism despite an underestimation of currents. In this section, the model is used to characterize (i) the variability of circulation on the scale of a M2 tidal cycle (the main component in the region), (ii) the Eulerian and (iii) Lagrangian residual currents involved in the transport of properties on longer time scales.

#### 3.5.1. Surface circulation

Tidal surface currents during spring tide are shown for a tidal cycle (from 0:00 to 10:00 on 08/02/19) (Fig. 6). We focus on flood (Fig. 6a), ebb (Fig. 6d) and intermediate situations (Fig. 6b,c,e,f). At t = 0:00, currents were oriented upstream (eastward) throughout the estuary, with maximum zonal velocities of ~60 cm $s^{-1}$ near the narrowest areas of the estuary (near the mouth; 16.6W–16.4W; between 16.35W and the eastern end of the domain; Fig. 6a). At t = 2:00 (Fig. 6b) the current reversed to the west and this reversal propagated from west to east: the current was weak near 16.55°W at 2:00 and near 16.3W at 4:00. At t = 6:00 (Fig. 6c), the flow was seaward across the entire domain, with maximum velocities of ~60 cm $s^{-1}$ near Karabane and Pointe Saint-Georges (PSG; 16.55°W). The same tidal surface current structure was observed during neap tides, with intensities ~50% lower than during spring tides (Fig. S6).

#### 3.5.2. Vertical structure of the current

Fig. 7 shows the vertical structure of the zonal current across a meridional section off Karabane Island (see red diamond indicating the section's longitude in Fig. 1) during spring tides. The strongest currents were found in the deeper sector (~10 m) of the channel. The current was sheared when its intensity was highest during ebb (Fig. 7b) and flood (Fig. 7e), with a velocity of ~36 cm $s^{-1}$ at the surface and ~15 cm $s^{-1}$ at the bottom. On the other hand, the current was relatively barotropic when weaker (Fig. 7d). Similar vertical structure and circulation, albeit less sheared, were observed in the neap period (Fig. S7). As off Karabane, the horizontal current off Ziguinchor was sheared and more intense at the surface above the river's maximum depth (~7 m in the model; Figs. S8 and S9). It should be noted that the 200 m horizontal resolution did not allow for fine representation of the Casamance topography and coastline in this sector of the river (*i.e.,* only 6 grid points are present in the section). This limitation could induce additional lateral friction (*e.g.,* Adcroft and Marshall, 1998) and reduce modelled velocities.

**Table 4**
Sea level amplitude (in cm) and phase (in degrees) of M2, M4 and M6 tidal waves at Karabane and Ziguinchor, using model output (reference simulation) and observations. Amplitude and phase were computed using t_tide. (M4/M2) amplitude ratio r and phase delay $\delta\varphi=(2\varphi M2-\varphi M4)$ were computed to evaluate tidal asymmetry. Errors are shown in parenthesis.

| | | Ziguinchor | | Karabane | |
|---|---|---|---|---|---|
| | | Model | Obs | Model | Obs |
| Amplitude (cm) | M2 | 20.9 (0.1) | 25.7 (0.3) | 55.7 (0.1) | 56.4 (0.6) |
| | MS4 | 0.6 (0.1) | 2.2 (0.3) | 0.6 (0.2) | 1.4 (0.7) |
| | M6 | 0.03 (0.1) | 1.2 (0.2) | 0.02 (0.1) | 1.1 (0.6) |
| | M4 | 1.1 (0.07) | 3.8 (0.08) | 1.1 (0.2) | 1.8 (0.6) |
| | r = a(M4)/a (M2) | 0.05 (0.1) | 0.14 (0.1) | 0.02 (0.1) | 0.03 (0.3) |
| Phase (°) | M2 | 169.5 (0.3) | 190.3 (0.6) | 106.5 (0.3) | 97.6 (0.6) |
| | M4 | 103.3 (4.9) | 33.5 (4.3) | 326.2 (8.2) | 169.3 (20.6) |
| | $\delta\varphi = 2\varphi M2-\varphi M4$ | 235.7 (5.6) | 347.1 (5.6) | 247.0 (8.5) | 25.9 (21.9) |

#### 3.5.3. Eulerian residual currents

The Eulerian residual current ($\mathbf{u}_E$) is the consequence of non-linear hydrodynamics. $\mathbf{u}_E$ is calculated by averaging instantaneous velocities over time T:

$$\vec{U}_E = \frac{1}{T}\int_{t_o}^{t_o+T} \vec{u}\left(\vec{x}_o, t\right) dt \quad (2)$$

where T is the averaging period, **u** the instantaneous current at the fixed position $x_0$ at time t.

This definition cannot be used directly for a signal composed of several harmonics. However, by averaging the simulated tidal current over a period of time much longer than the tidal periods, we can estimate the residual current. Here the residual circulation was calculated over a period of 176.4 days (*i.e.,* 12 times the spring to neap period of 14.7 days, between January 1st, 2015 and June 26th, 2015) for the reference simulation (note that very similar Eulerian currents were obtained with different averaging periods of the same length).

The depth-averaged Eulerian residual circulation was generally seaward in the estuary (Fig. 8a). Towards the river mouth, the westward current turned south-westward and intensified. A cyclonic (resp. anticyclonic) recirculation took place to the south (resp. north) of the mouth (16.8–16.75°W). Maximum residual current velocity was around 5 cm $s^{-1}$ between PSG and Ziguinchor. A cyclonic recirculation was also found in a deeper portion of the estuary west of PSG (~16.62°W; Fig. 8c).

To isolate the effect of the tides on the residual currents, the latter were computed over the same duration (176.4 days) from the sensitivity simulations with tidal forcing only (*i.e.,* "noatm" simulation; see Table 1; Fig. S10) and without tide (*i.e.,* "notide" simulation; Fig. 8b). The spatial patterns of the tidal residual current in the "noatm" simulation were similar to those of the reference simulation, with seaward velocity locally intensified. In contrast, the residual circulation driven by the atmospheric forcing ("notide" simulation) displayed several circulation cells: two elongated residual circulation cells with upstream (eastward) current over the shoals and seaward (westward) current in the deeper river bed (between sections S1-S2 and S3-S4; Fig. 8b), and two smaller circulation cells with upstream (north-eastward) current in the deeper river bed and a downstream (southwestward) current over the shoals (between S2-S3; Fig. 8b). As the wind direction veered progressively from southward (January) to eastward (June), these patterns have similarities with those forced by landward wind in shallow, elongated bays (F-Pedrera Balsells et al., 2020).

Fig. 9 illustrates the vertical structure of the Eulerian residual zonal current and its variability along the river (see sections in Fig. 8b). At the river mouth (Fig. 9a), seaward currents (~1–3 cm $s^{-1}$) were observed in the center of the channel and landward currents (~2–3 cm $s^{-1}$) along the edges. A convergence of the meridional currents led to a downwelling above the river's southern margin (~12.555°N). By contrast, off

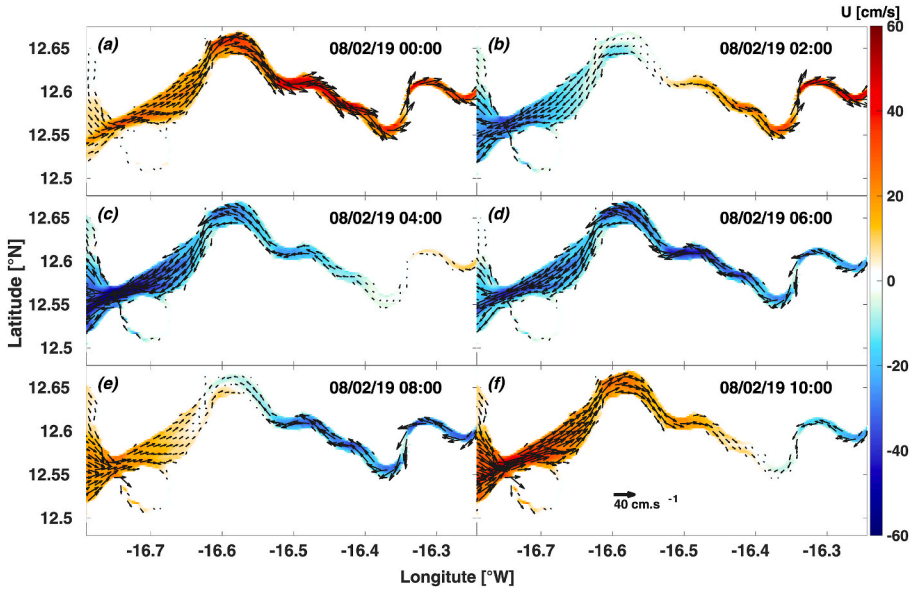


**Fig. 6.** Evolution of surface currents (in cm $s^{-1}$; vectors) and zonal velocity (in cm $s^{-1}$; color shading) over a tidal cycle (0:00–10:00; February 08, 2019) during spring tides. (For interpretation of the references to color in this figure legend, the reader is referred to the Web version of this article.)

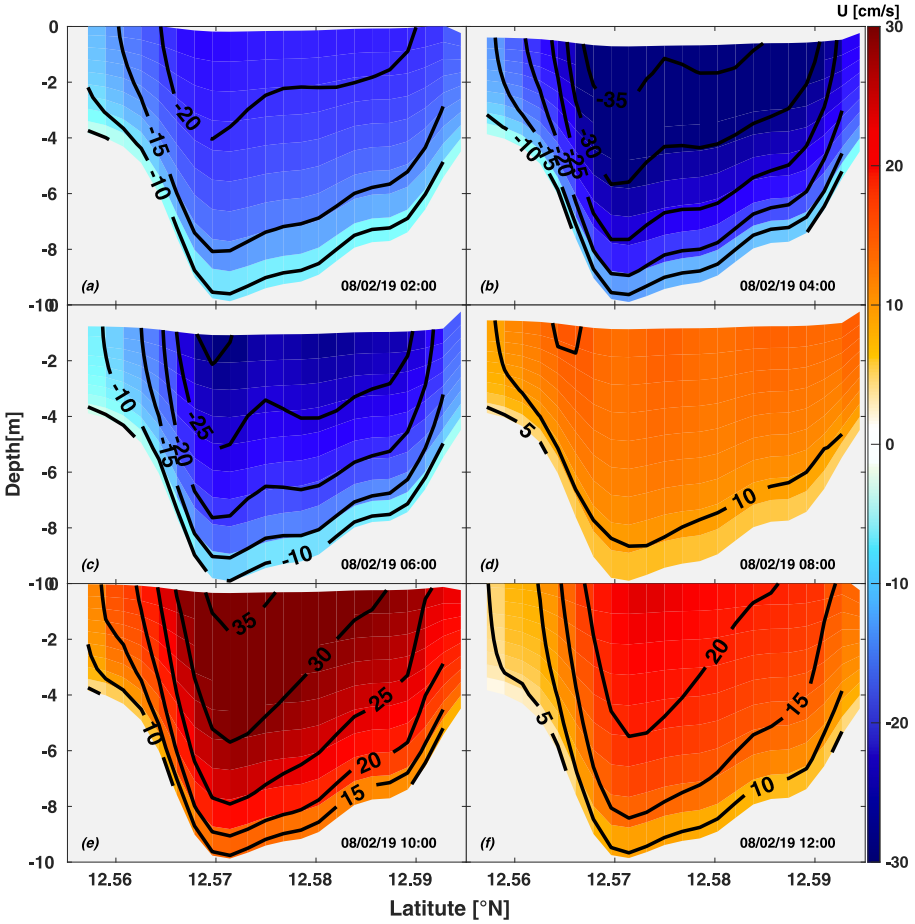


**Fig. 7.** Evolution of the vertical structure of the zonal current (in cm $s^{-1}$; color shading) at Karabane over a tidal cycle (2:00–12:00; February 08, 2019) during spring tide. (For interpretation of the references to color in this figure legend, the reader is referred to the Web version of this article.)

Karabane (Fig. 9b), the zonal residual current was predominantly seaward along the river margins and landward in a narrow (~600 m wide), band in the middle and deeper part of the channel. Outflow velocities were more intense (~1–3 cm $s^{-1}$) along the south bank than along the north bank, with downwelling occurring over the southern margin and upwelling occurring along the north bank. At PSG (Fig. 9c),

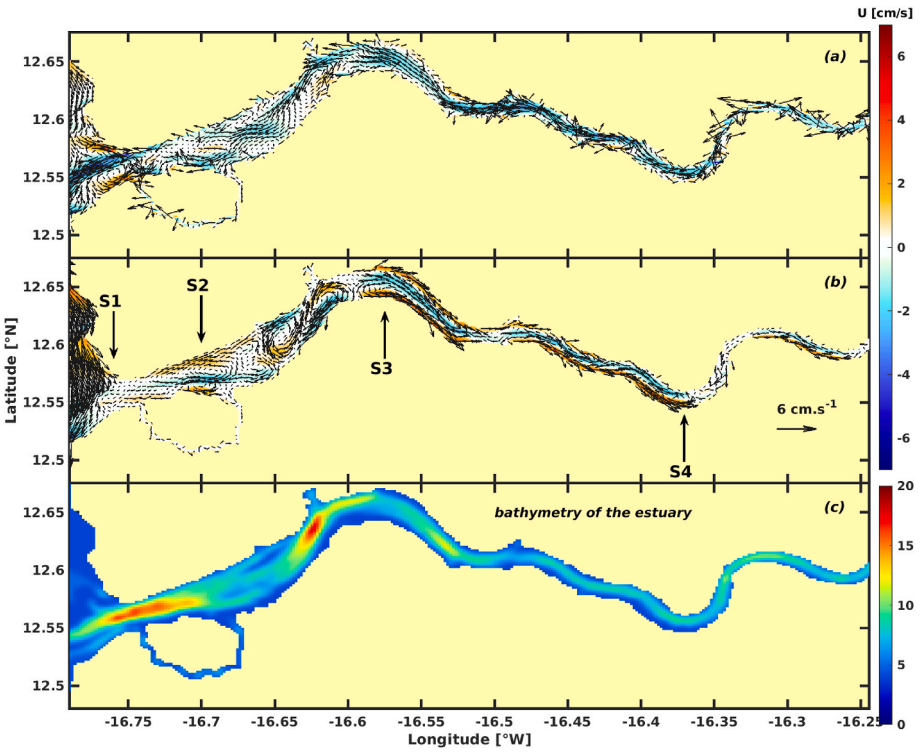


**Fig. 8.** Eulerian depth-averaged residual currents (in cm $s^{-1}$; vectors) and depth-averaged zonal velocity (in cm $s^{-1}$; color shading) for (a) the reference simulation and (b) the wind-driven, "notide" simulation (see Table 1). Currents were averaged over 6 lunar cycles (176.4 days, from January 1st, 2015–0:30 to June 26th, 2015–10:30). Meridional sections (S1-S4) shown in Fig. 9 are indicated by black arrows in (b). (c) Model bottom topography (in meters). (For interpretation of the references to color in this figure legend, the reader is referred to the Web version of this article.)

the circulation was similar to that at the river mouth, with a residual seaward current in most of the estuary, and a landward current along the river banks, particularly near the north bank. A similar current structure was found further east (16.37W; Fig. 9d), with seaward flow in the center of the channel, landward flow on the south bank and upwelling (resp. downwelling) along the north bank (resp. above the southern margin) of the river. Note that these circulation patterns may be modified in the presence of strong buoyancy gradients along the estuary, during the dry and rainy seasons.

### 3.5.4. *Lagrangian residual circulation*

The mean Lagrangian current $\mathbf{u}_L$ is defined as follows:

$$\overrightarrow{u_L} = \frac{1}{nT}\int_{t_o}^{t_o+nT} \overrightarrow{u}[\overrightarrow{x}(\overrightarrow{x_o}, t), t]\mathrm{d}t \quad (3)$$

with $T$ the tidal period, $\mathbf{x}_0$ the initial position of a water parcel and $\mathbf{x}$ the position of the water parcel at time $t$.

A long (one month) Lagrangian simulation (see section 2.5) was first carried out to illustrate the horizontal and vertical displacements of 12 water parcels in selected regions of the estuary (Fig. 10). An average seaward displacement of the released particles was found between the river mouth and the east of Karabane Island (~16.5°W). Near the river mouth, particles oscillated zonally under the effect of tidal currents, before being transported offshore and southward. A wide range of vertical displacements was observed (Fig. 10b): some particles (*e.g.,* #12) oscillated strongly vertically, between the surface (~0.5 m) and 15.5 m depth, while others (#5, #3 and #2) remained close to the surface. Particles (*e.g.,* #9 and #11) released off the river mouth (~7–10m), sank to 6.5m and 8m respectively. Particles released in the eastern part of the estuary (16.5–16.2W) got rapidly stranded (*e.g.,* #1,#2,#4) to the east of their initial position, suggesting a landward Lagrangian transport. Note that two particles released north of Karabane Island (#7 and #8) and offshore of the river mouth (#10) circulated clockwise around the Island, consistently with the Eulerian residual circulation (Fig. 8a).

The Lagrangian residual current field forced by tidal forcing (*i.e.,* obtained with the "noatm" simulation) is shown in Fig. 11. The vectors were averaged over a large number of experiments (see section 2.5) to filter numerical noise. The Lagrangian current was mainly landward in the estuary, with intensities of the order of 0.1–0.5 cm $s^{-1}$, and seaward at a few locations near the coast (*e.g.,* along the north bank between the river mouth and 16.55°W). The circulation was clockwise around Karabane Island. Near the river mouth, the circulation was inland and weak along the north bank and seaward along the south bank. The residual Lagrangian current may depend on the phase of the dominant tidal harmonic (M2 in the present case). However, in the present case, the velocity patterns were qualitatively similar in tidal phases 0h and 6h (Fig. S12).

Overall, the patterns of Lagrangian residual circulation were very different from those of the Eulerian residual circulation (Fig. 8a). the Lagrangian currents were much slower than the Eulerian ones, with maximum velocities of ~0.5–1 cm $s^{-1}$ and ~4–6 cm $s^{-1}$, respectively. The Lagrangian circulation was generally oriented landward and the Eulerian seaward, except at a few locations. Moreover, the topographically-related mesoscale structures visible in the Eulerian currents were not found in the Lagrangian flow. The Lagrangian current fields were also smoother in space than their Eulerian counterparts, a result consistent with hydrological modeling in other estuaries (*e.g.,* Minh et al., 2014; Zheng et al., 2003). The flushing time ($T_f$) of the estuary was particularly long (~600 days), consistently with the weak Lagrangian currents. $T_f$ was estimated by fitting the concentration of a passive tracer whose initial concentration was 1 in the estuary and 0 elsewhere to a decreasing exponential $m(t) = m(0).\exp(-t/T_f)$, *e.g.*, Das et al. (2000). After 300 days, ~60% of the total tracer mass initially in the estuary was still present in the estuary (Fig. S13).

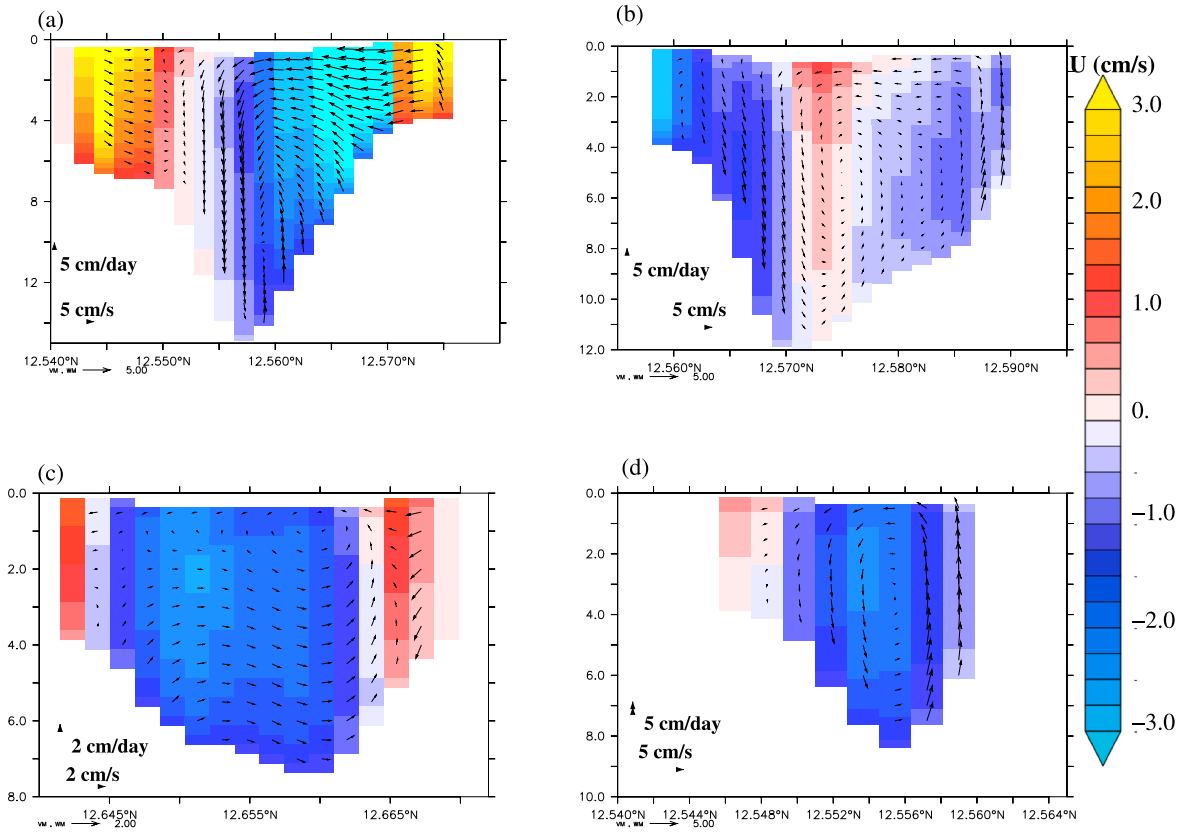


**Fig. 9.** Eulerian residual zonal (in cm $s^{-1}$; color shading), meridional and vertical velocities (arrows; note different scales for meridional and vertical velocities) (a) near the mouth (16.76°W; S1), (b) at Karabane (16.7°W; S2), (c) near Pointe-Saint-Georges (16.575°W; S3) and (d) at Ziguinchor (13.37°W; S4). The location of the meridional sections is indicated in Fig. 8b. Currents were averaged over 6 lunar cycles (176.4 days, from January 1st, 2015–0:30 to June 26th, 2015–10:30). (For interpretation of the references to color in this figure legend, the reader is referred to the Web version of this article.)

## 4. Discussion

### 4.1. Impact of friction

Bottom friction coefficients (Cd) were calculated using Wall's law (see equation (1)) with a fixed roughness length throughout the domain ($Z_o$ = 80 mm). The highest values (Cd~$2.10^{-1}$) were found in the shallow areas along the plateaus north and south of the mouth and along the south bank of the Casamance (Fig. S14). Such values are much higher than in most studies: for example, a spatially constant coefficient of the order of $10^{-3}$ (*e.g.,* $2.10^{-3}$ in the South China Sea; Fang et al., 1999; Cai et al., 2005) and lower roughness values (*e.g.,* $Z_o$ = 0.1 mm, Minh et al., 2014) were used. Nevertheless, values of Cd~ $10^{-2}$ have been estimated in regions of the China Sea (Qian et al., 2021) and in mangrove-lined regions in the Mekong Strait in Vietnam (Mullarney et al., 2017). The need for a high roughness length in our study could be due to the unaccounted frictional effect caused by mangroves on the river banks (Mazda, 2009). Furthermore, lateral friction in narrow straits of the estuary (discretized with only 4–5 ocean grid points in our configuration) may excessively reduce the horizontal current. Increasing horizontal resolution could alleviate this effect.

### 4.2. Underestimation of tidal currents

The model underestimated the tidal current intensity. There are several possible reasons for this. It may be due to imperfect topography dating back to 2012, which has probably changed due to silting. In addition, there might be vertical referencing errors in the original datasets used in GEBCO, which might result in zeroth-order errors in the bathymetry off the river mouth (*e.g.*, the crescent-shape staircase in the merged product near 16.82°W, see Fig. S2). Such biases may result in a bias of the tidal energy flux radiated from the ocean into the estuary.

The very strong bottom friction we used (see section 4.1) is consistent with the underestimation of the current. The use of spatial variation in roughness length ($Z_o$) could improve our results. In addition, Zheng et al. (2003) showed that the use of wet and dry parameterization to represent intertidal salt marshes (unaccounted for in our simulations) could also improve the realism of the velocities, increasing them by ~50% in their case study. A better knowledge of the river bathymetry would enable us to test the impact of this parametrization. Increasing the vertical resolution (i.e., using 20 vertical levels instead of 10) had a negligible impact on the amplitude of the currents. Vertical mixing of momentum may also play a role: other turbulence schemes implemented in CROCO (*e.g.,* the Generic Length Scale scheme) could be tested, which is beyond the scope of the present work.

### 4.3. Discrepancies in observed and modelled tidal asymmetry

Weak asymmetries in the duration of observed sea level rise (flood) and fall (ebb) were found, whereas flood dominance (*i.e.,* shorter flood than ebb) was found in the simulations. These discrepancies suggest that the realism of our model needs to be improved to represent non-linearities in a more realistic manner. Furthermore, the modelled asymmetry was not consistent with that obtained following Friedrichs and Aubrey (1988)'s approach. Discrepancies with their approach were found in other studies. For example, in the Charente estuary, Friedrichs and Aubrey (1988)'s approach predicted ebb dominance, whereas observations indicated shifts from flood to ebb-dominance during the spring to neap tide transitions (Toublanc et al., 2015). Using a model, these authors showed that nonlinear interactions between M2 and S2 did

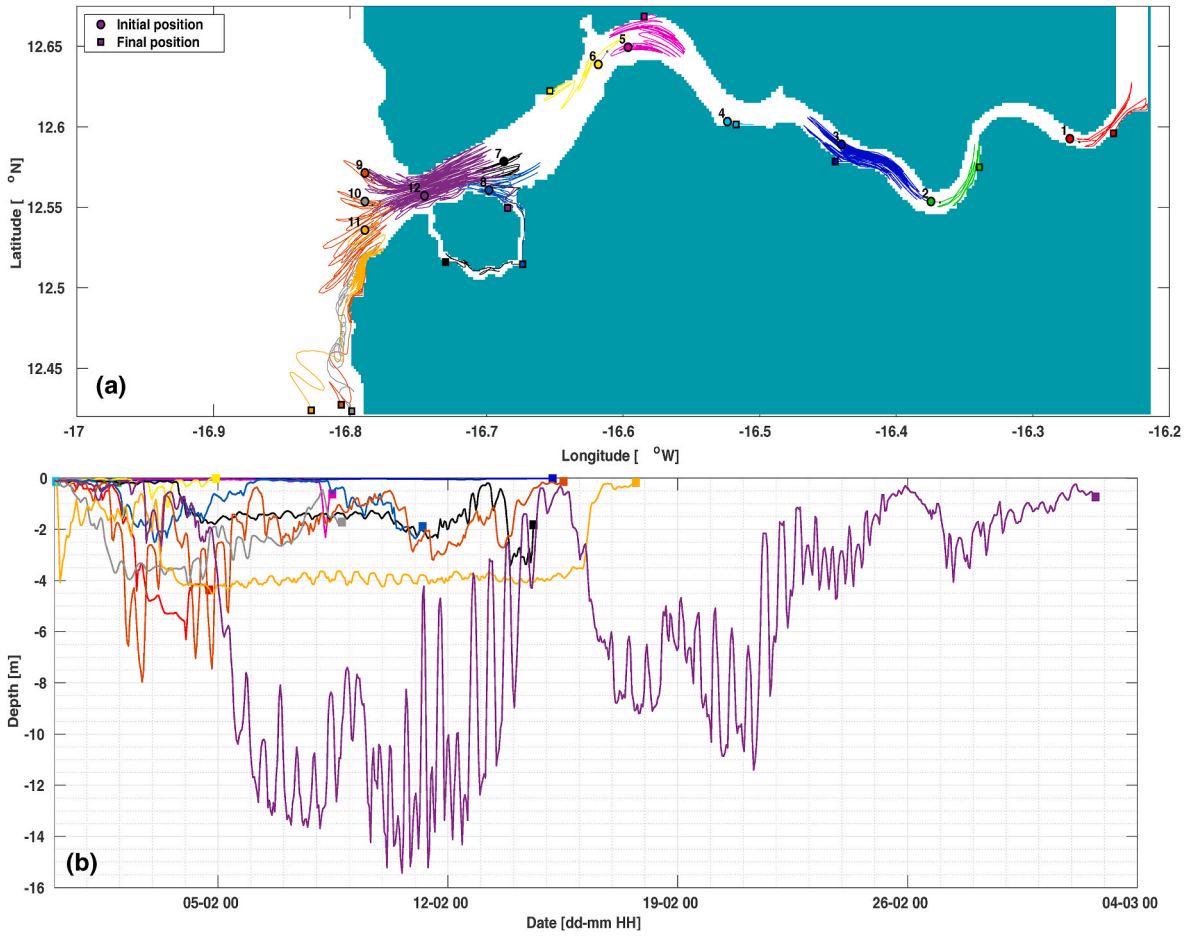


**Fig. 10.** (a) Pathways of Lagrangian particles released near the surface (at 0.1 m depth) on February 1st (reference simulation). (b) Vertical displacement of the particles. Colored circles and squares represent initial and final positions, respectively.

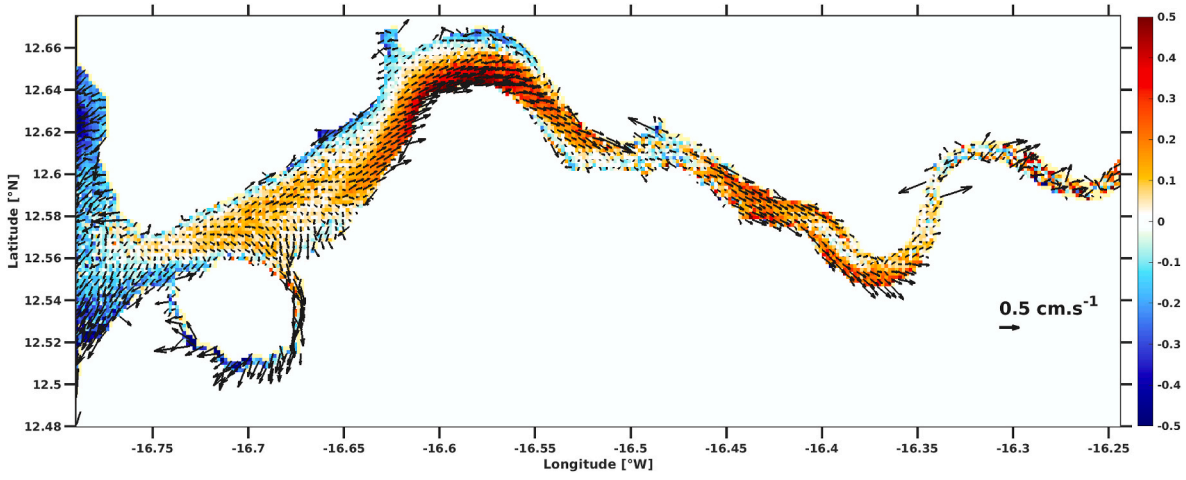


**Fig. 11.** Lagrangian surface currents (in cm $s^{-1}$, vectors) and zonal current (in cm $s^{-1}$, color shading) for the reference simulation. The surface drifts from 800 Lagrangian experiments launched every 3 h for a duration of 14.7 days (half a lunar month) were averaged (see section 2.5). Note the different vector scale from that of the residual Eulerian currents (Fig. 8). (For interpretation of the references to color in this figure legend, the reader is referred to the Web version of this article.)

not reproduce the observed asymmetry, but that it was correctly simulated when the M2,S2 and M4 were imposed at the model boundaries, allowing complex interactions between these three harmonics. Investigating the drivers of asymmetry with our model would necessitate running additional simulations with different selections of harmonics at the boundaries, which is beyond the scope of the present work.

### 4.4. Eulerian residual circulation

The theory of tidal residual circulation in the presence of variable topography has been well established (*e.g.,* Zimmerman, 1980; Li and O'Donnel, 1997). The residual current generally flows along isobaths, leaving shallow depths to its right in the northern hemisphere. This is

consistent with the simulated cyclonic structure near PSG (~16.62°W; Fig. 8a) and west of Karabane Island (~16.75°W). Other mechanisms, such as the effect of coastal curvature, could also play a role.

The residual Eulerian circulation in the Casamance estuary bears similarities with that in other estuaries, *e.g.,* the Satilla River estuary (Zheng et al., 2003). Despite a weaker residual surface current in the Casamance River (~6 cm $s^{-1}$; Fig. S11) than in the Satilla River (~20 cm $s^{-1}$ in the M2 tide only experiment), the circulation in both estuaries was mainly directed seaward. Several cyclonic and anticyclonic structures were also found in the Satilla River, with converging and diverging currents at the river edges generating downwelling and upwelling.

The vertical structure of the residual current (Fig. 9) can also be compared to theoretical results from Burchard et al. (2011) (hereafter BU2010). In this study, the authors used an idealized model of tidal flow with invariant width and depth in the river direction, a fixed salinity gradient along the river and no runoff. The vertical structure of the three-dimensional current depended strongly on two dimensional parameters, the relative buoyancy parameter (or Simpson parameter) $Si = \partial_x b.\ (H/U^*)^2$ and the unsteadiness parameter $U_n = \omega\ (H/U^*)$, with b the buoyancy defined as $b = -g\ (\rho-\rho_0)/\rho_0$, $H$ the estuary depth, $\partial_x b$ the buoyancy longitudinal gradient, ω the tidal frequency, and U* the bottom friction velocity. U* was evaluated using the following formula: $Cd=(U^*/U_T)^2$, $U_T$ being the tidal velocity scale. Using Cd~0.05 (see Fig. S14), $U_T$ = 0.5 m/s, $\partial_x b = -(g/\rho_0).\partial_x \rho$, H = 10 m for the Karabane section (16.7°W), we obtained Si~0.4 and $U_{\tilde{n}}$0.05. The Casamance case is therefore comparable to the "Large Si" case (Si~0.2; $U_{\tilde{n}}$0.03) in BU2010. In this particular case, the eastward velocity was maximal in the center of the channel and near the bottom, with surface velocities oriented westward at the edges (see Fig. 8c from BU2010), which resembled the residual current at Karabane (Fig. 9b). Lateral surface currents converged, giving rise to downwelling in the center of the channel, similar to our model results. According to BU2010, upstream bottom velocity near the center of the channel is mainly related to tidal straining, due to differences in vertical mixing of horizontal momentum between flood (strong mixing of upstream momentum) and ebb (weak mixing of downstream momentum). In our simulation, the weak landward current near the bottom may be due to a weak seaward density gradient associated with the dry season (no freshwater runoff) and also to the meridional asymmetry of the channel near Karabane Island. Note that including river runoff (~50–100 $m^3/s$ from the GloFAS product; Harrigan et al., 2020) in the reference simulation thereby increasing the seaward buoyancy gradient by nearly a factor 10 did not significantly modify the residual current's patterns (not shown).

Using an analytical model, Li and O'Donnel (1997, 2005) studied the subtidal residual circulation in an idealized channel of arbitrary length. They found residual Eulerian currents landward at the edges and seaward at the center near the river mouth (see Fig. 9a) of a "long" channel (*i.e.,* when the channel length is larger than one quarter of the gravity wave length $\lambda=(gH)^{1/2}/f$; Li and O'Donnel, 2005). This corresponds to the case of the Casamance River. According to these authors, this exchange flow results from the competition between several mechanisms. An inflow is caused by non-linearities associated with the surface fluctuations of the progressive tidal wave and with bottom friction. Consequently, a seaward residual pressure gradient is required to push water out for the mass balance to equilibrate (see mean sea level in Fig. S15). Since the surface elevation in a narrow estuary such as the Casamance had little lateral variation (*e.g.,* see the weak lateral variations of amplitude and phase in Fig. 5), the longitudinal pressure force integrated over depth is mainly depth-dependent. It is therefore greater in the channel than over the shoals, thus a greater return flow occurs in the channel than over the shoals. The net effect of these tidal non-linearities is a landward flow on the river shoals and a seaward flow in the middle of the channel.

### 4.5. Contrasting Eulerian and Lagrangian residual circulations

The Lagrangian residual circulation obtained in our simulations is the sum of Eulerian residual flow and Stokes drift driven by gravity waves. As the modelled tidal currents were underestimated, non-linearities hence residual currents may be larger in the real estuary. Comparison of the Eulerian (Fig. 8) and Lagrangian (Fig. 11) circulations showed significant differences, in particular that the Lagrangian circulation was much weaker (~1 cm $s^{-1}$) than the Eulerian circulation (~4–6 cm $s^{-1}$). Stokes drift, which was not explicitly calculated in our study, therefore tended to oppose Eulerian circulation in most of the estuary. Li and O'Donnel (1997, 2005) calculated a "first-order" estimation (*e.g.,* with respect to a small parameter $\varepsilon = |\zeta|/H \ll 1$; ζ and H are sea level and water column thickness, respectively) of the Stokes drift as $U_T = <\zeta.U>/H$ (U is the depth-averaged velocity and brackets mark time averaging over a tidal period). In our study case, the "first-order" Stokes drift was landward (easward) everywhere in the estuary and locally intensified (Fig. S16), thus tended to compensate the (mostly seaward) Eulerian residual velocity. However the total residual circulation (*i.e.,* the sum of Eulerian and "first-order" Stokes drift, or "transport velocity"; Fig. S16; Li and O'Donnel (1997)) was much larger than the Lagrangian circulation derived from the drifter trajectories (Fig. 11). It is therefore likely that the higher-order terms neglected in the decomposition play a important role.

Such differences between Lagrangian and Eulerian residuals have also been found in various coastal regions (*e.g.,* Zheng et al. (2003) in the Satilla River estuary; Wei et al. (2004) in the Bohai Sea; Wang et al. (2013) in the southwestern yellow sea; Rodríguez et al. (2017) in the Gulf of California). In the Satilla River estuary, Zheng et al. (2003) found that the weak residual Lagrangian current was due to the strong nonlinearity of the tidal current, the Stokes current being of the same order of magnitude and opposite direction to the Eulerian current. As the Stokes drift can also be due to surface waves, studying the impact of surface wave forcing on the Lagrangian current (*e.g.,* Marchesiello et al., 2019; Sow et al., 2021) would be an interesting perspective. Finally, as only the residual circulation during the dry season (*i.e.,* without river flux) was characterized, it would be interesting to carry out a similar study in the rainy season in the presence of downstream freshwater flow.

## 5. Conclusions and perspectives

The Casamance estuary tidal sea level variations and circulation were studied using numerical modeling. A regional configuration of the CROCO model was set up, using the observed bathymetry in the western part of the estuary and supplementing the eastern part with an idealized channel of constant depth. The model was forced at the open boundaries by 8 diurnal (K1, O1, P1, Q1) and semi-diurnal (M2, S2, N2 and K2) tidal waves from the TPXO7 global tidal model. Particular attention was paid to evaluating the regional model using coastal satellite altimetry and in-situ sea level data, and current meter data. Using a logarithmic friction profile allowing for spatial variation in bottom friction coefficient, the regional model was calibrated using a set of sensitivity experiments to adjust the roughness length. It reproduced the sea level variations (amplitude and phase) associated with the tide with an acceptable level of realism, implying that the global model provided an adequate boundary forcing for the regional model. An underestimation of current intensity was nevertheless observed. The tidal surface current had a similar spatial structure during spring and neap tides, with a 50% reduction in intensity during neap tides. The Eulerian residual current was mainly seaward while the Lagrangian residual current was weaker and mainly landward. The weak intensity of the Lagrangian residual circulation indicated significant compensation by the Stokes drift.

The study has many prospects. As the limitations of the model remain substantial, it is necessary to continue improving it and evaluating its realism with new observations. This will be done by collecting new current measurements, temperature and salinity data within the estuary.

A new model configuration needs to be developed, using a more complete bathymetry including intertidal salt marshes and representing the river to the east of Ziguinchor and the main tributaries. It is also be important to study the effect of the tide on salinity variations during the dry season (*i.e.,* with stronger longitudinal salinity gradients in the estuary than the ones in these simulations) and during the rainy season by taking into account the seaward flow of fresh water. Implementing a freshwater flux at the air-sea interface instead of a virtual salt flux (which is acceptable in the open ocean; Roullet and Madec, 2000) may also be necessary to simulate the inward water flux at the estuary mouth during the dry season. Benefiting from CROCO facilities, our simulations may be used to study the residual transport of sediment, contaminants (using a passive tracer) and fish eggs and larvae (*e.g.,* using the Ichthyop Lagrangian tool, Lett et al., 2008). This will be particularly useful in the recent context of hydrocarbon extraction off Senegal (Gueye et al., 2016).

## CRediT authorship contribution statement

**Birane Ndom:** Writing – review & editing, Writing – original draft, Visualization, Validation, Software, Methodology, Investigation, Conceptualization. **Siny Ndoye:** Writing – review & editing, Writing – original draft, Supervision, Conceptualization. **Bamol Ali Sow:** Writing – review & editing, Writing – original draft, Supervision, Conceptualization. **Vincent Echevin:** Writing – review & editing, Writing – original draft, Supervision, Methodology, Investigation, Conceptualization.

## Declaration of competing interest

The authors declare that they have no known competing financial interests or personal relationships that could have appeared to influence the work reported in this paper.

## Acknowledgements

Birane Ndom was funded by the PDI-ARTS program from the Institut de Recherche pour le Développement (IRD) and by LMI ECLAIRS2. Vincent Echevin was supported by IRD and by the LEFE-GMMC program (COCASAM project). Siny Ndoye was supported by Université Amadou Mahtar Mbow (UAM) and Bamol Sow by Université Assane Seckh (UAS). Siny Ndoye and Bamol Sow would like to thank IRD for the "Sud-Nord" funding and the LMI ECLAIRS2. Numerical simulations were carried out as part of DARI projects A9_1140, A11_1140 and A13_1140 on the Jean-Zay supercomputer at IDRIS. The authors thank Luc Descroix for sharing pressure data, Eric Machu and Xavier Capet for sharing ADCP measurements, Patrick Marchesiello and Issa Sakho for fruitful discussions.

## Appendix A. Supplementary data

Supplementary data to this article can be found online at https://doi.org/10.1016/j.csr.2024.105389.

## Data availability

Data will be made available on request.

## References

Adcroft, A., Marshall, D., 1998. How slippery are piecewise-constant coastlines in numerical ocean models? Tellus Dyn. Meteorol. Oceanogr. 50 (1), 95–108.
Barnier, B., Siefridt, L., Marchesiello, P., 1995. Thermal forcing for a global ocean circulation model using a three-year climatology of ECMWF analyses. J. Mar. Syst. 6, 363–380. https://doi.org/10.1016/0924-7963(94)00034-9.
Birol, F., Fuller, N., Lyard, F., Cancet, M., Nino, F., Delebecque, C., Fleury, S., Toublanc, F., Melet, A., Saraceno, M., Léger, F., 2017. Coastal applications from nadir altimetry: example of the X-TRACK regional products. Adv. Space Res. 59, 936–953. https://doi.org/10.1016/j.asr.2016.11.005.
Blayo, E., Debreu, L., 2005. Revisiting open boundary conditions from the point of view of characteristic variables. Ocean Model. 9 (3), 231–252.
Brak, R., Cordier, S., Jillings, T., 2013. Development of port of ziguinchor | RVO.nl | Rijksdienst. https://www.rvo.nl/subsidies-regelingen/projecten/development-port-ziguinchor.
Brunet-Moret, Y., 1970. Etudes des marées dans le fleuve Casamance : Rapport définitif-fdi:04581- Horizon. https://www.documentation.ird.fr/hor/fdi:04581.
Burchard, H., Hetland, R.D., Schulz, E., Schuttelaars, H.M., 2011. Drivers of residual estuarine circulation in tidally energetic estuaries: straight and irrotational channels with parabolic cross section. J. Phys. Oceanogr. 41, 548–570.
Da Silva, A.M., Young, C.C., Levitus, S., 1994. Atlas of surface marine data 1994. Algorithms and procedures, technical report, Natl. Oceanogr. and Atmos. Admin., Silver, Spring, Md 1.
Das, P., Marchesiello, P., Middleton, J.H., 2000. Numerical modelling of tide-induced residual circulation in sydney harbour. Mar. Freshw. Res. 51, 97–112.
Debreu, L., Marchesiello, P., Penven, P., Cambon, G., 2012. Two-way nesting in split-explicit ocean models : algorithms, implementation and validation. Ocean Model. 49–50, 1–21. https://doi.org/10.1016/j.ocemod.2012.03.003.
Descroix, L., Sané, Y., Thior, M., Manga, S.-P., Ba, B.D., Mingou, J., Mendy, V., Coly, S., Dièye, A., Badiane, A., Senghor, M.-J., Diedhiou, A.-B., Sow, D., Bouaita, Y., Soumaré, S., Diop, A., Faty, B., Sow, B.A., Machu, E., Vandervaere, J.-P., 2020. Inverse estuaries in west Africa : evidence of the rainfall recovery? Water 12 (3), 647. https://doi.org/10.3390/w12030647.
Dinapoli, M.G., Simionato, C.G., Moreira, D., 2020. Nonlinear tide-surge interactions in the Río de la Plata Estuary. Estuar. Coast Shelf Sci. 241, 106834. https://doi.org/10.1016/j.ecss.2020.106834.
Diombéra, M., 2010. Aménagement et gestion touristique durable du littoral sénégalais de la Petite Côte et de la Basse Casamance. Thèse de doctorat en tourisme. Saint-Louis (Sénégal) :Université Gaston Berger, p. 343.
Diouf, P.S., Pagès, J., Saos, J.-L., 1986. Géographie de l'estuaire de la Casamance, 11.
Egbert, G.D., Erofeeva, S.Y., 2002. Efficient inverse modeling of barotropic ocean tides. J. Atmos. Ocean. Technol. 19 (2), 183–204.
F-Pedrera Balsells, M., Grifoll, M., Espino, M., Cerralbo, P., Sánchez-Arcilla, A., 2020. Wind-driven hydrodynamics in the shallow, micro-tidal estuary at the fangar bay (Ebro delta, NW mediterranean sea). Appl. Sci. 10, 6952. https://doi.org/10.3390/app10196952.
FAO, 2011. Aperçu du développement rizicole au Sénégal. Division de la production végétale et de la protection des plantes (AGP) de la FAO. Bureau Afrique de l'Ouest, Dakar, p. 10.
Friedrichs, C.T., Aubrey, D.G., 1988. Nonlinear tidal distortion in shallow well-mixed estuaries: a synthesis. Estuar. Coast Shelf Sci. 27, 521–545. https://doi.org/10.1016/0272-7714(88)90082-0.
Gebco, G. B. C., 2021. GEBCO_2021 Grid (World). British Oceanographic Data Centre. https://doi.org/10.5285/c6612cbe-50b3-0cff-e053-6c86abc09f8f.
Geyer, W.R., MacCready, P., 2014. The Estuarine circulation. Annu. Rev. Fluid Mech. 46, 175–197. https://doi.org/10.1146/annurev-fluid-010313-141302.
Gueye, A., Klof, S., Thiaw, M., Faye, S., Mbaye, A., Ndoye, S., Capet, X., Diop, A., Brehmer, P., 2016. Discovery of oil and gas in Senegal: marine environment, protected fishing areas and marine protected areas. Advocacy for collective prevention of ecological risks. ICAWA International Conference, The AWA PROJECT : Ecosystem Approach to the management of fisheries and the marine environment in West African Waters. https://horizon.documentation.ird.fr/exl-doc/pleins_textes/divers18-01/010072144.pdf.
Harrigan, S., Zsoter, E., Alfieri, L., Prudhomme, C., Salamon, P., Wetterhall, F., Barnard, C., Cloke, H., Pappenberger, F., 2020. GloFAS-ERA5 operational global river discharge reanalysis 1979–present. Earth Syst. Sci. Data 12 (3), 2043–2060.
Hersbach, H., Bell, B., Berrisford, P., et al., 2020. The ERA5 global reanalysis. Q. J. R. Meteorol. Soc. 146, 1999–2049. https://doi.org/10.1002/qj.3803.
Hilt, M., Roblou, L., Nguyen, C., Marchesiello, P., Lemari e, F., Jullien, S., Dumas, F., Debreu, L., Capet, X., Bordois, L., Benshila, R., Auclair, F., 2020. Numerical modeling of hydraulic control, solitary waves and primary instabilities in the Strait of Gibraltar. Ocean Model. 151 (16p), 101642. https://doi.org/10.1016/j.ocemod.2020.101642.
Lahoud, A., 1989. Modélisation des circulations transitoire et résiduelle : Application à l'estuaire de la Casamance (Sénégal) Thèse de l'. Academie de Montpellier. Universite des Sciences et Techniques du Languedoc. https://horizon.documentation.ird.fr/exl-doc/pleins_textes/pleins_textes_7/TDM_7/26512.pdf.
Large, W.G., McWilliams, J.C., Doney, S.C., 1994. Oceanic vertical mixing: a review and a model with a nonlocal boundary layer parameterization. Rev. Geophys. 32, 363–403. https://doi.org/10.1029/94RG01872.
Largier, J.L., 2023. Recognizing low-inflow estuaries as a common estuary paradigm. Estuar. Coast 46, 1949–1970. https://doi.org/10.1007/s12237-023-01271-1.
Le Reste, L., 1982. Variations spatio-temporelles de l'abondance et de la taille de la crevette Penaeus notialis en Casamance (Sénégal). Oceanologica Acta, Special issue 6.
Lett, C., Verley, P., Mullon, C., Parada, C., Brochier, T., Penven, P., Blanke, B., 2008. A Lagrangian tool for modelling ichthyoplankton dynamics. Environ. Model. Software 23 (9), 1210–1214. https://doi.org/10.1016/j.envsoft.2008.02.005.
Levitus, S., Locarnini, R.A., Boyer, T.P., Mishonov, A.V., Antonov, J.I., Garcia, H.E., Baranova, O.K., Zweng, M.M., Johnson, D.R., Seidov, D., 2010. World Ocean Atlas 2009. National Oceanographic Data Center (U.S.), Ocean Climate Laboratory,;United States, National Environmental Satellite, Data, and Information Service. https://repository.library.noaa.gov/view/noaa/1259.
Li, C., O'Donnel, J., 1997. Tidally drive, residual circulation in shallow estuaries with lateral depth variation. J. Geophys. Res. 102.

Li, C., O'Donnel, J., 2005. The effect of channel length on the residual circulation in tidally dominated channels. J. Phys. Oceanogr. 35, 1826–1840.
Longuet-Higgins, M.S., 1969. On the transport of mass by time-varying ocean currents. Deep Sea Res. 16, 431–447.
Marchesiello, P., McWilliams, J.C., Shchepetkin, A., 2001. Open boundary condition for long-term integration of regional oceanic models. Ocean Model. 3, 1–21.
Marchesiello, P., Nguyen, N.M., Gratiot, N., Loisel, H., Anthony, E.J., Dinh, C.S., Nguyen, T., Almar, R., Kestenare, E., 2019. Erosion of the coastal Mekong delta : assessing natural against man induced processes. Continent. Shelf Res. 181, 72–89. https://doi.org/10.1016/j.csr.2019.05.004.
Mazda, Y., 2009. In: Perillo, Gerardo M.E., Wolanski, Eric, Cahoon, Donald R., Brinson, Mark M. (Eds.), Hydrodynamics and Modeling of Water Flow in Mangrove Areas. Coastal Wetlands: an Integrated Ecosystem Approach, 2009. Elsevier, p. 231.
Millet, B., Olivry, J.-C., Letroquer, Y., 1986. Étude du fonctionnement hydrologique de la Casamance maritime. In: Reste Louis, Le, André, Fontana, Samba, A. (Eds.), L'estuaire de la Casamance : environnement, pêche, socio-économie. Dakar : ISRA/CRODT, pp. 23–37.
Minh, N.N., Marchesiello, P., Lyard, F., Ouillon, S., Cambon, G., Allain, D., Van Uu, D., 2014. Tidal characteristics of the gulf of Tonkin. Continent. Shelf Res. 91, 37–56. https://doi.org/10.1016/j.csr.2014.08.003.
Mullarney, J.C., Henderson, S.M., Reyns, J.A.H., Norris, B.K., Bryan, K.R., 2017. Spatially varying drag within a wave-exposed mangrove forest and on the adjacent tidal flat. Continent. Shelf Res. 147, 102–113.
Ndoye, S., 2016. Fonctionnement dynamique du centre d'upwelling sud- sénégalais: approche par la modélisation réaliste et l'analyse d'observations satellite de température de la mer. PhD thesis Université Pierre et Marie Curie. https://theses.hal.science/tel-01481384/file/2016PA066372.pdf.
Ndoye, S., Capet, X., Estrade, P., Sow, B., Machu, E., Brochier, T., Döring, J., Brehmer, P., 2017. Dynamics of a "low-enrichment high-retention" upwelling center over the southern Senegal shelf. Geophys. Res. Lett. 44. https://doi.org/10.1002/2017GL072789.
Nuñes, R.A., Lennon, G.W., Bowers, D.G., 1990. Physical behaviour of a large, negative or inverse estuary. Continent. Shelf Res. 10 (3), 277–304.
Parker, B.B., 1991. The relative importance of the various nonlinear mechanisms in a wide range of tidal interactions. In: Parker, B. (Ed.), Tidal Hydrodynamics. John Wiley, pp. 237–268.
Pawlowicz, R., Beardsley, B., Lentz, S., 2002. Classical tidal harmonic analysis including error estimates in MATLAB using T_TIDE. Comput. Geosci. 28 (8), 929–937. https://doi.org/10.1016/S0098-3004(02)00013-4.
Penven, P., Marchesiello, P., Debreu, L., Lefèvre, J., 2008. Software tools for pre- and post-processing of oceanic regional simulations. Environ. Model. Software 23, 660–662. https://doi.org/10.1016/j.envsoft.2007.07.004.
Piton, V., Ouillon, S., Vinh, V.D., Many, G., Herrmann, M., Marsaleix, P., 2020a. Seasonal and tidal variability of the hydrology and suspended particulate matter in the Van Uc estuary, Red River, Vietnam. J. Mar. Syst. https://hal.archives-ouvertes.fr/hal-03053185.
Piton, V., Herrmann, M., Lyard, F., Marsaleix, P., Duhaut, T., Allain, D., Ouillon, S., 2020b. Sensitivity study on the main tidal constituents of the Gulf of Tonkin by using the frequency-domain tidal solver in T-UGOm. Geosci. Model Dev. (GMD) 13 (3), 1583–1607.
Qian, S., Wang, D., Zhang, J., Li, C., 2021. Adjoint estimation and interpretation of spatially varying bottom friction coefficients of the M 2 tide for a tidal model in the Bohai, Yellow and East China Seas with multi-mission satellite observations. Ocean Model. 161, 101783. https://doi.org/10.1016/j.ocemod.2021.101783.
Rickerich, S., Ross, L., Valle-Levinson, A., 2022. Wave enhanced overtides in an idealized tidal inlet system. J. Geophys. Res.: Oceans 127, e2022JC018848.
Risien, C.M., Chelton, D.B., 2008. A global climatology of surface wind and wind stress fields from eight years of QuikSCAT scatterometer data. J. Phys. Oceanogr. 38, 2379–2413.
Rodríguez, P.B., Carbajal, N., Heberto Gaviño Rodríguez, J., 2017. Lagrangian trajectories, residual currents and rectification process in the Northern Gulf of California, Estuarine. Coastal and Shelf Science 194, 263–275. https://doi.org/10.1016/j.ecss.2017.06.019.
Roullet, G., Madec, G., 2000. Salt conservation, free surface, and varying levels: a new formulation for ocean general circulation models. J. Geophys. Res.: Oceans 105 (C10), 23927–23942. https://doi.org/10.1029/2000JC900089.
Savenije, H.G., Pagès, J., 1992. Hypersalinity: a dramatic change in the hydrology of the Sahelian estuaries. J. Hydrol. 135 (Issues 1–4), 157–174. https://doi.org/10.1016/0022-1694(92)90087-C.
Schoellhamer, D.H., 2000. Influence of salinity, bottom topography, and tides on locations of estuarine turbidity maxima in northern San Francisco Bay. In: McAnally, W.H., Mehta, A.J. (Eds.), Proceedings in Marine Science, 3. Elsevier, pp. 343–357. https://doi.org/10.1016/S1568-2692(00)80130-8.
Sène, A.M., Diémé, I., 2018. Entre développement touristique et recul des espaces rizicoles dans la commune de Diembéring (région de Ziguinchor) : quelle alternative pour un développement local durable? BELGEO. http://journals.openedition.org/belgeo/23362.
Shchepetkin, A.F., McWilliams, J.C., 2005. The regional oceanic modeling system (ROMS) : a split-explicit, free-surface, topography-following-coordinate oceanic model. Ocean Model. 9 (4), 347–404. https://doi.org/10.1016/j.ocemod.2004.08.002.
Sow, M., Chevalier, C., Sow, B., Pagano, M., Devenon, J.-L., 2021. Coupled effects of tide and swell on water renewal in a meso-tidal channel lagoon : case of the Toliara Lagoon (Madagascar). Estuar. Coast Shelf Sci. 259, 107463. https://doi.org/10.1016/j.ecss.2021.107463.
Toublanc, F., Brenon, I., Coulombier, T., Le Moine, O., 2015. Fortnightly tidal asymmetry inversions and perspectives on sediment dynamics in a macrotidal estuary (Charente, France). Continent. Shelf Res. 94, 42–54. https://doi.org/10.1016/j.csr.2014.12.009.
von Karman, Th, 1931. Mechanical Similitude and Turbulence, Tech. Mem. NACA no. 611, 1931.
Wang, B., Hirose, N., Moon, J.H., Yuan, D., 2013. Difference between the Lagrangian trajectories and Eulerian residual velocity fields in the southwestern Yellow Sea. Ocean Dynam. 63, 565–576.
Wei, H., Hainbucher, D., Pohlmann, T., Feng, S., Suendermann, J., 2004. Tidal-induced Lagrangian and eulerian mean circulation in the Bohai Sea. J. Mar. Syst. 44 (3–4), 141–151.
Zheng, L., Chen, C., Liu, H., 2003. A modeling study of the Satilla River estuary, Georgia. I: flooding-drying process and water exchange over the salt marsh-estuary-shelf. Complex Estuaries 26 (3), 651–669.
Ziegler, F., Eichelsheim, J.L., Emanuelsson, A., Flysjö, A., Ndiaye, V., Thrane, M., 2009. Life Cycle Assessment of southern pink shrimp products from Senegal. An environmental comparison between artisanal fisheries in the Casamance region and a trawl fishery based in Dakar. SIK report 789.
Zimmerman, J.T.F., 1980. Vorticity transfer by tidal currents over an irregular topography. J. Mar. Syst. 38, 601–630.